Energy Conversion and Management 252 (2022) 115109

Contents lists available at ScienceDirect

Energy Conversion and Management

journal homepage: www.elsevier.com/locate/enconman

Flow visualisation in real-size optical injectors of conventional, additised, and renewable gasoline blends

Milad Heidari-Koochi [a,*], Ioannis K. Karathanassis [a,b], Phoevos Koukouvinis [a,b], Joonsik Hwang [c], Lyle M. Pickett [b], David Spivey [d], Manolis Gavaises [a]

[a] School of Mathematics, Computer Science and Engineering, City, University of London, Northampton Square EC1V 0HB London, UK
[b] Combustion Research Facility, Sandia National Laboratories, 7011 East Avenue, Livermore, CA 94550, USA
[c] Centre for Advanced Vehicular Systems (CAVS), Department of Mechanical Engineering, Mississippi State University, Starkville, MS 39762, USA
[d] Lubrizol European Research and Development Centre, Nether Lane, Hazelwood DE56 4AN Derby, UK

ARTICLE INFO

Keywords:
GDI engine
Diffuse Backlight Illumination
High-speed imaging
Viscoelastic flow
Gasoline/ethanol blend

ABSTRACT

Research on renewable and alternative fuels is crucial for improving the energy and environmental efficiency of modern gasoline internal combustion engines. To highlight the influence of fuel rheological and thermodynamic properties on phase change and atomisation processes, three types of gasoline blends were tested. More specifically, the campaign comprised a reference gasoline, an ethanol/gasoline blend (10% v/v) representative of renewable fuels, and an additised gasoline sample treated with viscoelasticity-inducing agents. High-speed imaging of the transient two-phase flow field arising in the internal geometry and the near-nozzle spray region of gasoline injectors was performed employing Diffuse Backlight Illumination. The metallic body of a commercial injector was modified to fit transparent tips realising two nozzle layouts, namely a two-hole real size model resembling the Engine Combustion Network spray G injector and an enraged replica with an offset hole. Experiments were conducted at realistic operating conditions comprising an injection pressure of 100 bar and ambient pressures in the range of 0.1–6.0 bar to cover the entire range of chamber pressures prevailing in Gasoline Direct Injection engines. The action of viscoelastic additives was verified to have a suppressive effect on in-nozzle cavitation (6% reduction in cavitation extent) , while also enhancing spray atomisation at flash-boing conditions, in a manner resembling the more volatile gasoline/ethanol blends. Finally, persisting liquid ligaments were found to form after the end of injection for the additised sample, owing to the surfactant nature of the additives.

1. Introduction

Active research on a cleaner combustion is vital to render modern internal-combustion engines compliant with the stringent emissions legislation to be imposed in Europe and the U.S. within the next decade. Albeit the shift to passenger-car electrification is precipitated by governmental incentives, the process is expected to be time-consuming and spanning across at least 30 years [1]. Urgent societal and environmental concerns about the use of fossil fuels and after-effects on climate change dictate the rapid development of internal combustion engines with enhanced fuel efficiency and reduced emissions primarily operating with renewable fuels. The substitution of fossil by renewable fuels has become an urgent necessity stemming from concerns regarding the depletion of natural resources and requirements for energy security, as well as a small reduction in carbon dioxide (CO_2) emissions. Ethanol (C_2H_5OH) has been widely used in Europe and the US for blending with commercial gasoline, owing to its chemical compatibility with conventional fuel and the fact that, in principle, it can be produced in a sustainable manner. So called, first-generation ethanol can be produced from sugar cane, corn, [2] or switchgrass [3], whereas second-generation, in order to reduce the competition with food crops, is produced from biomass processing to release the sugars in cellulose and hemicellulose of plant material, which, in turn, can be fermented to provide ethanol [4]. A number of studies in the literature focus on the evaluation of the combustion characteristics of gasoline-ethanol blends, in terms of power output [5,6] and emissions [7]. Ethanol, due to its high activation energy, increases the octane rating of the fuel. Hence, higher compression ratios are allowed, owing to higher resistance to engine knock, leading to higher thermodynamic efficiency [8].

* Corresponding author.
E-mail address: Milad.Heidari-Koochi@city.ac.uk (M. Heidari-Koochi).

https://doi.org/10.1016/j.enconman.2021.115109
Received 11 August 2021; Received in revised form 2 December 2021; Accepted 3 December 2021
Available online 11 December 2021

Nomenclature

d	orifice diameter, m
n	sample size
p_{amb}	ambient pressure, Pa
Re	Reynolds number
t	time, s
t^*	normalised time
t_{tot}	total injection duration, s
u	Velocity, m/s
Greek symbols	
α	probability
ν_f	fuel kinematic viscosity, m^2/s
ρ_f	fuel density, kg/m^3
σ	standard deviation

Gasoline/ethanol blends at concentrations up to up to 10% v/v have been found to be compatible with existing combustion systems [9]. It should also be noted that addition of small percentages of ethanol in the fuel has a moderate reducing effect in terms of CO_2 emissions [9].

An understanding of Gasoline Direct Injection (GDI) spray dynamics is critical when addressing several topics in state-of-the-art engines including stratified/homogeneous charge strategies [10], advanced compression ignition [11], avoidance of wall-wetting [12], and injection strategies [13]. Poor fuel spray atomisation and impingement on the cylinder walls lead to poor combustion efficiency and eventually increased emissions [14,15]. It has become well established in the relevant literature that the performance of the fuel injection system has a crucial influence on the efficiency of GDI engines. In pursuit of improving combustion efficiency and reducing pollutants emissions, numerous studies have been conducted on injector designs [16], enhancing fuel atomisation, vaporisation, and mixing processes in the engine cylinder [17–19]. Focusing on flow processes associated with fuel injection, the morphology of the expelled spray has been proven to be closely linked to the complex two-phase flow field arising within the injector sac and nozzle holes. Transient, in-nozzle cavitation has been verified to occur in both diesel [20,21] and gasoline injectors [22]. Depending on its morphological features and dynamic evolution, the onset of cavitation can have either a detrimental or a beneficial impact on the device performance and reliability, by inducing erosion [23,24] and reduced or variable fuel delivery [25,26] regarding the former case or enhancing fuel break up and spray atomisation with regards to the latter [27,28].

The utilisation of transparent injector tips fitted to modified bodies of metallic injectors constitutes a widely adopted practice for the visualisation of in-nozzle cavitating flow. The numerous studies available in the literature refer to both real-size tips [29], as well as enlarged nozzle replicas [30], which facilitate the cavitating structures to be resolved with higher spatial resolution [31]. Flow similarity despite the variation in characteristic length scales is ensured through matching of non-dimensional quantities characterising the prevailing flow conditions, such as the Reynolds, Weber, and Cavitation numbers.

Investigations at conditions relevant to GDI engines have been conducted incorporating transparent tips of different layouts, as well as a range of multi-component gasoline blends and single-component surrogates. Gilles-Birth et al. [32] elucidated the characteristics of in-nozzle cavitation in a real-size, single-hole valve-covered orifice (VCO). Injection and ambient pressures lied in the ranges of 20–80 bar and 1–16 bar, respectively. The variation of injection and back-pressures allowed the visualisation of incipient, film, and vortical cavitation with an explicit correlation to the spray-cone temporal variation. Serras-Pereira et al. [28] performed flash-boiling experiments in a transparent single-hole injector. Gasoline and two single-component surrogates, namely *iso*-octane and n-pentane, were injected at a pressure of 23 bar and temperatures between 20 and 90 °C in ambient with pressures between 0.5 and 1.0 bar. The flow visualisation demonstrated that increase in the degree of superheat leads to significantly enhanced primary break-up and finer spray atomisation, as vapour bubbles forming within the nozzle acted as perturbations triggering flash vaporisation of low boiling-point components. In a parallel work from the same group, Aleiferis et al. [8] included bio-derived components in the experimental matrix, namely, ethanol, butanol (C_4H_9OH), and a gasoline-ethanol, E10 blend alongside the aforementioned fuels. It was found out that increasing the gasoline temperature, increased the levels of in-nozzle cavitation which resulted in producing asymmetry in the injected sprays. E10 behaved similar to gasoline in almost all test conditions having slightly wider spray plumes. N-pentane (C_5H_{12}) was found to have the most in-nozzle cavitation compared to the other fuels. Finally, for both ethanol and butanol, no significant differences were observed in the in-nozzle cavitation when the fuel temperature was increased from 20 °C to 50 °C. Jiang et al. [33] proposed a method based on optical imaging to quantify in nozzle cavitation composition in terms of volume fraction. A comparative study was conducted on the influence of injection pressure and nozzle geometry for multi-component gasoline and an E15 gasoline/ethanol blend. It was discovered that the mean volume fraction of the in-nozzle cavitation during the injection period was 15% higher in E15 in comparison with the reference gasoline (EEE fuel). Moreover, the impact of fuel properties on cavitation was stronger at early stages of injection where reference gasoline caused the cavitation to appear earlier than E15 due to its lower viscosity and higher saturation pressures. Mamaikin et al. [34] studied the internal flow of a real size two-hole transparent nozzle. Gasoline was injected at pressures up to 100 bar into a pressure chamber at atmospheric pressure. Using an ultra-high-speed imaging technique at 5 MHz the formation and development of the in-nozzle string cavitation were observed. Moreover, a micro Particle Image Velocimetry (PIV) method was also applied to extract the velocity distribution of the internal flow. Hwang et al. [35] carried out high-speed extinction imaging in a real-size axial-hole transparent nozzle to assess the near nozzle behaviour of flashing sprays. N-pentane at room temperature and pressurised at 100 bar was injected into a sealed vessel realising ambient to fuel saturation pressures in the range of 0.07–1.39. The authors quantified the composition of the expelled spray in terms of projected liquid volume for a variety of conditions, from flare flashing boiling to non-boiling.

Phase-change processes in the cylinders of gasoline engines range from flash boiling to pure evaporation and therefore, apart from the design of fuel injection equipment, the thermodynamic and transport properties of the fuel itself have a strong influence on the atomisation quality [36]. With regards to renewable fuels, Mohammed et al. [37] studied the effects of ethanol/gasoline blends on exhaust gas emissions at different engine speeds (1500–2500 rpm) of a one-cylinder, four-stroke spark ignition engine. Ethanol was mixed with gasoline at different proportions to achieve four blends of E10, E20, E30, and E40. The examination of emission characteristics showed that exhaust gas emissions such as unburnt hydrocarbons (HC), nitrogen oxides (NO_x), CO_2, and carbon monoxide (CO) were significantly reduced by increasing the ethanol content of gasoline fuel. The maximum drop in CO emissions was found in E30 by 26%, while E40 exhibited the lowest reduction in CO_2 emissions by 25%. Similarly, E40 showed lower HC and NO_x emissions compared to the gasoline by 31% and 21%, respectively. Iodice et al. [38] performed an experiment to investigate the influence of ethanol–gasoline blended fuels on cold emissive behaviour of a four-stroke Spark Ignition (SI) engine. The results showed that E10 had a 15% reduction of CO emission in comparison with the reference gasoline. As the addition of ethanol increases the oxygen content of the blend, an improvement in the combustion process is expected which subsequently reduces carbon monoxide emission. With regards to unburnt hydrocarbons, E10 exhibited 24% less HC compared to the

reference gasoline which is once more due to a higher oxygen content that results in an improved oxidation of unburnt hydrocarbons. It may be worth mentioning that two unattractive features associated with the use of ethanol in gasoline blends, namely that it has a lower heating value and stoichiometric air to fuel ratio compared to gasoline [39] and that it is water soluble. Bioethanol usually contains about 5% water after the fermentation process, which must be removed before blending with gasoline [40].

The use of additives to boost octane rating and antiknock properties of the fuel also constitutes a common industrial practice to enhance engine performance and reduce emissions [41]. Besides, additives acting as detergents have been used extensively in commercial gasoline fuels to reduce the formation of deposits forming on several components of the fuel delivery system and leading to power loss, reduced engine efficiency and increased emissions [42]. The exact chemical composition of such additives and their influence on the rheological behaviour of the fuel are usually aspects of proprietary research [43], hence the information available in the open literature is quite fragmented across different research topics. Relevant to this work are polymeric additives inducing a viscoelastic behaviour to the flow. Viscoelasticity has been primarily linked with turbulent drag reduction and subsequent pressure loss suppression in single-phase flows [44,45]. Flexible polymeric chains absorb energy from turbulent eddies and disrupt the turbulence-cascade sequence to small scales, thus, increasing flow efficiency [46]. Nevertheless, investigations on the interaction of viscoelasticity with cavitating structures and, especially those relevant to high-speed injector flows are quite rare. Naseri et al. [47] carried out high-speed X-ray imaging experiments on an enlarged replica of a diesel injector, as well as Large Eddy Simulations (LES) [48] in a realistic device geometry, employing a viscoelastic diesel blend. The experiments and simulations confirmed that viscoelasticity suppresses wall-attached cavitation, while also reducing the overall in-nozzle magnitude of turbulence. In an additional work from the same group, Karathanassis et al. [49] employed X-ray phase contrast imaging to illustrate the influence of viscoelasticity on the topology and dynamics of cavitation developing inside an enlarged replica of a diesel fuel injector. Placement of the static needle to distinct lift values enabled the manifestation of different cavitation regimes, namely cloud and vortical cavitation. The x-ray data confirmed that in the presence of viscoelasticity-inducing agents, cloud cavitation was suppressed, while the opposite was true for vortex-induced cavitation.

Despite the numerous studies reporting the effect of gasoline fuel blends and injection strategies on gasoline engine performance, there is nonetheless room for further evaluation of the influence of the fuel rheological and thermodynamic properties on fundamental flow processes associated with fuel injection. As the production of first- and second-generation biofuels, particularly ethanol blends of gasoline, comes with either extensive chemical processes and/or competition with food crops, introducing ppm concentrations of flow-enhancing viscoelasticity agents can be considered as an attractive alternative to increase the fuel efficiency of gasoline engines. To the authors' knowledge, the present work is the first in the open literature illustrating the influence of viscoelasticity on the cavitating flow arising in the internal geometry of gasoline injectors. It should also be pointed out that the viscoelasticity-inducing agent employed in this investigation, a Quaternary Ammonium Salt, has been proven to also act as a detergent dissolving injector deposits [50]. A comparative evaluation of the sample containing viscoelasticity-inducing agents against a reference gasoline and a gasoline/ethanol blend representative of renewable fuels allows distinct features regarding cavitation formation and spray atomisation to be highlighted. Flow visualisation has been performed in two-transparent tips, namely a two-hole, real-size, and an enlarged single-hole layout, with the latter facilitating the illustration of in-nozzle cavitation morphology.

2. Experimental setup

This section describes the equipment and methods incorporated to derive physical information from the obtained high-speed images. More specifically, the injection system and sealed chamber, as well as the fuel samples employed are discussed in sub-section 2.1. Subsequently, sub-section 2.2 focuses on the optical setup realised and image-processing techniques utilised in this investigation.

2.1. Injection system and pressure chamber

A sealed cubical chamber with a characteristic dimension of 63.5 mm, as shown in Fig. 1**a**, was used for the flow visualisation campaign. Dual-view optical access was enabled by four ports bearing fused silica windows, 25 mm in diameter each. The ambient pressure within the vessel was regulated through valve-controlled nitrogen supply, channelled into the chamber by four intake lines located at its top corners. The fuel and nitrogen mixture was scavenged from the chamber by an exhaust pipe shown in the bottom part of Fig. 1**a**. Pressure transducers located at the intake line and exhaust lines were used to monitor and record the ambient pressure. For current experiments, the ambient pressure range lied in the range 0.1–6 bar, which is representative of the prevailing in-cylinder pressures during gasoline fuel injection. Sub-atmospheric conditions were obtained with the use of an oil-ring vacuum pump.

Fuel was injected in the sealed chamber with the use of a modified Bosch HDEV5 injector having its metallic tip machined off past the location of the needle seat to accommodate the optical tip. The injector and tip assembly were clamped onto a pedestal, bespoke for each tip layout, securing the optical injector within the vessel and the height of the window port and allowing the visualisation of the near-nozzle region due to its corrugated geometry. The injector needle was driven by an electronic driver giving a signal with a time duration of 0.68 ms. Although the actual hydraulic duration cannot be precisely determined for the optical injector, since the needle tip does not protrude into the active visualisation window, needle motion profile measurements for the HDEV5 injector are available as shown in Fig. 1**c**. The profile was measured through time resolved X-ray phase contrast imaging at the Advanced Photon Source (APS) of Argonne National Laboratory and corresponds to a hydraulic injection duration approximately equal to 780 μs [35]. More sophisticated, multiple-injection events, although relevant to GDI operation, were not considered as the main objective of the investigation is to elucidate the influence of fuel rheology and thermodynamic properties on in-nozzle and spray behaviour. A more complex injection event would come with the risk of making such effects more challenging to identify. Furthermore, successive injections would increase the risk of tip failure.

Fuel was pressurised to 100 bar at the injector inlet with the use of a high-pressure syringe pump, which, depending on the ambient pressure lead to indicative values of the Reynolds number characterising the in-nozzle flow reported in Table 1, along with the main parameters of the experiments. Injection pressure was maintained at 100 bar to ensure that the optical tips would not fail, owing to mechanical fatigue, throughout the entire investigation. It was deemed crucial to retain the same tip (per layout) for all test cases, as micro-fabrication imperfections between test-pieces would possibly obscure the comparison between different fuels and conditions. Besides, the ambient pressure range was selected so as to be comparable to the G condition variations, as identified for universal experimentation by the Engine Combustion Network (ECN) [51], which range from 0.5 bar to 6 bar and cover a wide range of gasoline-engines operation envelope spanning from early injection strategies at low load for homogeneous mixture formation to late-injection strategies under stratified engine operation. In an attempt to compensate for the low fuel temperature in the present experiments a deeper vacuum of 0.1 bar was selected to approach the flashing conditions at the end of intake stroke.

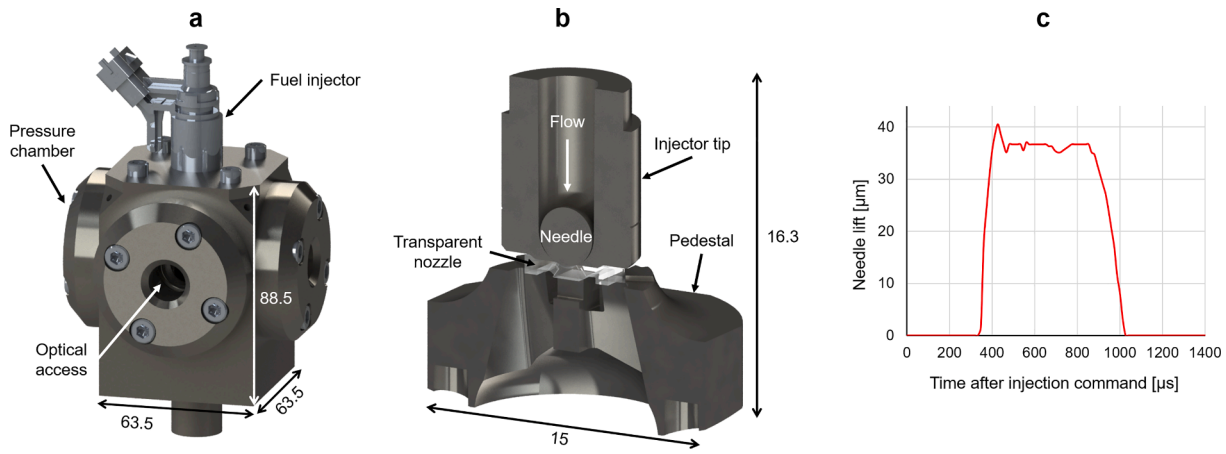

Fig. 1. a) External view of the sealed vessel with the injector being mounted at a vertical position. b) Section view of injector tip and transparent nozzle. c) Needle-lift profile of a metallic HDEV5 injector for an electronic pulse of 680 μs [35].

Table 1
Fuel properties and experimental conditions for the examined test cases. The Reynolds number was calculated as $Re = \frac{u \bullet d}{\nu_f}$ using the orifice diameter d, as a characteristic length scale and the fuel kinematic viscosity, ν_f. Thermodynamic and transport properties for the gasoline fuels used for the Reynolds definition were obtained from [55,56]. Indicative velocity values (u) were calculated using the Bernoulli equation between the injection and ambient pressures.

Fuel	Base gasoline	Additised gasoline	E10
ρ_f [kg/m^3]	741	741	746
Kinematic viscosity (m^2/s)	5.74×10^{-7}	5.74×10^{-7}	6.57×10^{-7}
Reid Vapour pressure ($\times 10^3$ Pa)	61.4	61.4	69.4
Re (Real size tip)	47,200–48,600	47,200–48,600	41,100–42,400
Re (Enlarged tip)	94,800–97,700	94,800–97,700	82,600–85,100
Ambient gas	N_2		
Ambient pressure ($\times 10^5$ Pa)	0.1–6.0		
Ambient temperature (K)	298		
Injection pressure ($\times 10^5$ Pa)	100		
Fuel temperature (K)	298		

Two injector layouts were fabricated from cast acrylic and employed in the comparative investigation of the different fuel samples. The first of those constitutes an enlarged single-hole orifice with a hemispherical upstream sac region, as depicted in Fig. 2**a**. The orifice hole has an offset of 170 μm from the symmetry axis of the sac in order to promote an asymmetrical cavitation cloud attached to the nozzle hole also showing propensity for cavity shedding, as has been verified in previous investigations employing mm-sized nozzles relevant to diesel fuel injection [52,53]. The second optical layout, shown in Fig. 2**b**, corresponds to a real-size injector with two counterbore holes resembling those of the actual Spray G injector employed for experimentation by the ECN [54]. The nozzles of the two-hole tip have a length-to-diameter ratio of 1.3 upstream the counterbore section of square cross section 390 μm × 390 μm, which extends to an additional 470 μm of length. Each hole has a 37° inclination angle (hole-axis angle) relative to the injector axis.

Three types of gasoline were comparatively assessed in the present experimental campaign. The samples comprised a standardised gasoline (Haltermann EEE fuel), referred to as '*base*' from now on, a base sample treated with Quaternary Ammonium Salts (QAS) at a concentration of 1000 mg/kg, '*additised*' henceforth, inducing a viscoelastic behaviour to the fluid and a 10% (v/v) ethanol/base blend (E10). Fuel samples were selected in such a manner to provide a comprehensive comparison between alternative fuel blends and commercial gasoline fuels, as well as widely adopted renewable counterparts. The suspension of QAS

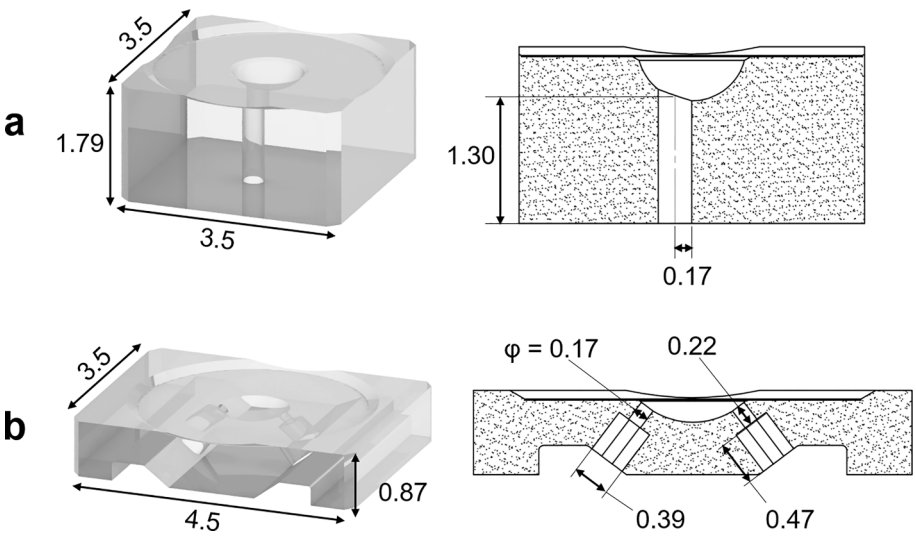

Fig. 2. External (left) and section (right) views of employed injector transparent tips: a) enlarged orifice and b) real-size two-hole layout. Dimensions are in mm.

additives in diesel fuel has been proven to lead to the formation of flexible micelles within the liquid fuel, which interact with vortical structures at different length scales [49]. Such interactions have an overall beneficial impact on fuel injection, in terms of in-nozzle flow efficiency and spray atomisation. An attempt to verify a similar influence with reference to gasoline fuel is attempted in this investigation. Fuel samples were kept at room temperature for the experiments since acrylic tips were employed, and their relevant bulk properties are summarised in Table 1, while the respective distillation curves are shown in Fig. 3. Prior measurements have verified that the addition of QAS additives does not affect the thermodynamic and transport properties of the reference gasoline fuel. In addition, 10% (v/v) ethanol/base gasoline constitutes a non-ideal mixture which produces the highest difference in Reid vapour pressure compared to base gasoline than higher percentages of ethanol, refer to. This makes E10 suitable to assess the influence of thermodynamic properties on fuel vaporisation.

2.2. Optical setup and high-speed images post-processing

An optical setup based on Diffuse Backlight Illumination (DBI), the schematic of which is shown in Fig. 4, was developed to be able to capture high-speed images of both the two in and near nozzle regions of the different injector layouts. Given the diffuse nature of the illumination sources, refractive index gradients captured in the images are owed solely to the presence of liquid/gas interfaces. Two high-speed cameras with CMOS sensors (Photron FASTCAM SA-X2 and Phantom v2512) in sync with pulsating Light Emitting Diodes (LEDs), namely a blue (wavelength of 455 ± 22 nm) and a red one (wavelength of 620 ± 19 nm), were employed to capture the injection events. Both cameras were fitted with long-distance microscopes (Infinity K2 DistaMax with CF-2 objectives) focused either on the internal nozzle flow path or the region downstream the nozzle outlet. In order to avoid wavelength cross-talk effects, respective bandpass filters were placed in front of the cameras. Furthermore, condensing lenses were placed in front of the LEDs to minimise the light spillage beyond the edges of the chamber optical windows. LEDs and cameras were simultaneously triggered by the injector driver with the light pulse being fired at mid-duration of the camera exposure time. Owing to the very rapid LED pulsation mode, nanosecond-long exposure times could be achieved ensuring that any blurriness was absent from the raw images. The visualisation settings applied for the experiments incorporating each one of the two transparent tips are summarised in Table 2.

Sequences of raw images captured for the two layouts during indicative injection events are shown in Fig. 5. As already mentioned, the offset in the geometry of the enlarged nozzle leads to the formation of an asymmetrical yet well-established cloud cavity, as depicted in Fig. 5**a**. The cloud is attached on the lower half of the nozzle cross-section and occupies its entire length, while dynamic vaporous structures prevail on the upper part of the cross-section throughout the

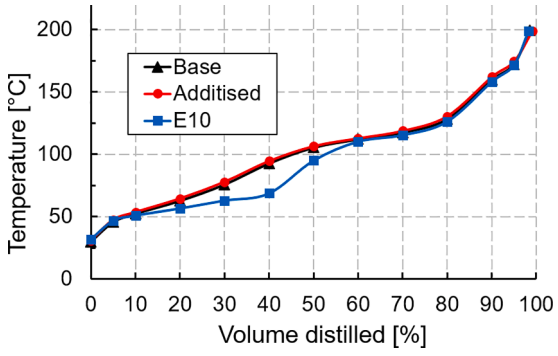

Fig. 3. Distillation curves of the three fuel samples examined, as determined by an ASTM D86 test [57].

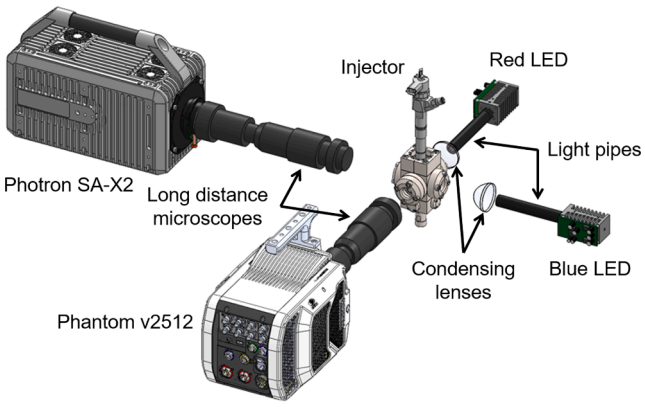

Fig. 4. Schematic of the optical set-up realised for the experiments. Both the in- and near-nozzle regions can be visualised concurrently by the two cameras owing to the dual-view optical access allowed by the chamber.

Table 2
Summary of visualisation settings for the conducted experiments.

Transparent-tip layout	Enlarged orifice		Two-hole real size
View orientation	Side view	Top view	Side view
Acquisition frequency (fps)	100,000	100,000	87,000
Exposure time	2 μs	250 ns	250 ns
Active window (pixel)	640 × 170	512 × 208	640 × 256
Active window (mm)	2.62 × 0.70	2.56 × 1.04	3.2 × 1.28
Spatial resolution (μm/pixel)	4.1	5.0	5.0

injection event. Top-view visualisation, as depicted in Fig. 5**b**, enabled the illustration of the topology and dynamics of vortical cavities arising in the hemispherical sac of the enlarged model. It should be noted that highly transient, elongated (string) cavities intermittently appear in the sac during the entire event for all the conditions examined. In addition, the top-view images illustrate the spray region with fidelity and fine features, such as satellite droplets detaching from the main plume can be discerned with clarity.

In a similar manner, Fig. 5**c** illustrates a sequence of raw images obtained for the two-hole transparent tip. Preliminary test cases have verified that extensive cavitation establishes in both nozzles and a two-phase mixture fills up the counterbore holes rendering them opaque. Likewise, the small depth of the sac did not allow light to penetrate in that region as well. Since visible light is susceptible to extensive scattering near wall boundaries, visualising regions of high curvature is not possible using optical imaging. Near-wall visualisation can be accomplished instead with the use of high-flux, i.e., synchrotron, radiation, for instance employing X-ray Phase Contrast Imaging, as the scattering angles of X-rays are significantly lower compared to light [53]. Hence, it was deduced that no appreciable quantitative information could be extracted from the internal flow-path region for the specific layout and the relevant analysis focused on near-nozzle atomisation and spray dynamics.

A series of image processing techniques was applied to extract quantitative information regarding the extent and evolution of the in-nozzle cavitation, as well as the topology and dynamics of the expelled fuel spray. As already mentioned, quantitative data regarding the in-nozzle extent of cavitation can be extracted only for the enlarged orifice and the relevant post-processing steps are highlighted in Fig. 6**a**. As a first step, raw images were subtracted by a background image, which was produced by averaging 50 images of the orifice occupied by stagnant liquid. Subsequently, an adaptive thresholding procedure based on Otsu's algorithm [58] was utilised to binarise the image. The final binarised image depicts the projected area of the vaporous structures arising within the nozzle. The same procedure was followed to

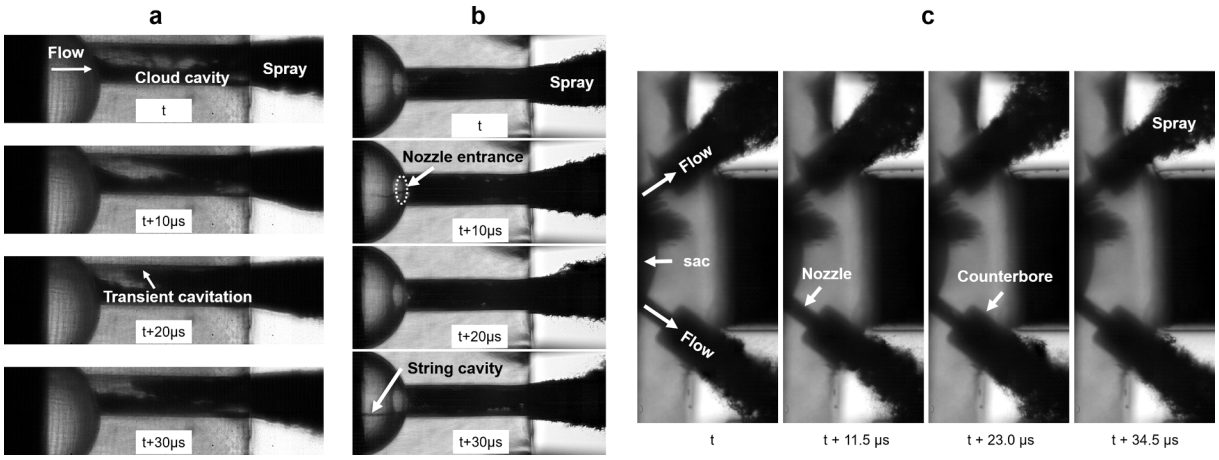

Fig. 5. Sequence of time instances referring to base gasoline at $P_{amb} = 1.0$ bar. a) Side view images illustrating the in-nozzle cavitation in the enlarge orifice, b) top view images illustrating vortical cavitation in the sac region and spray morphology in the near-nozzle region. c) Respective image sequence for the real-size two-hole injector tip with focus being given in the near-nozzle spray region. Flow is from left to right.

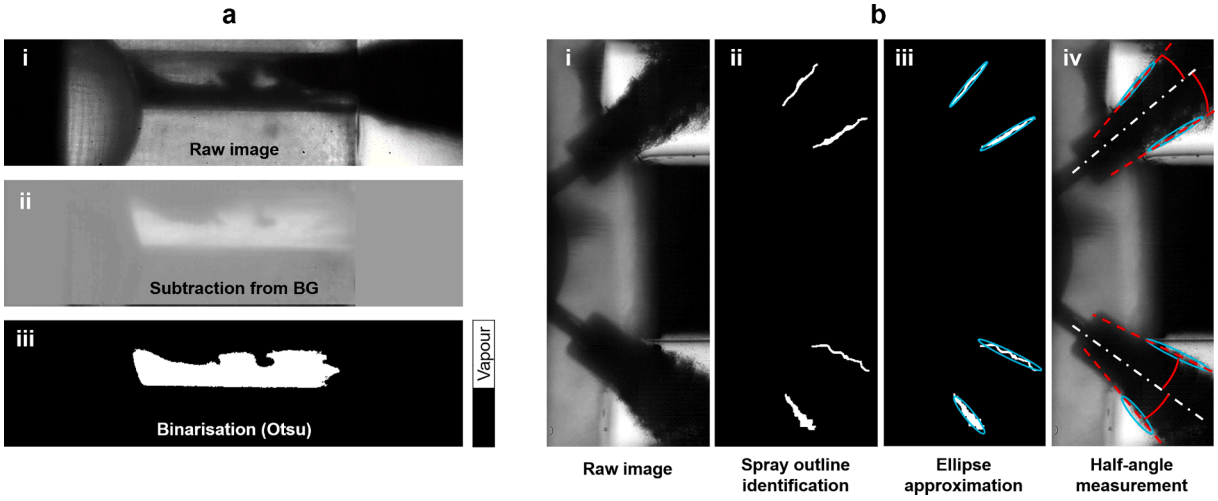

Fig. 6. Outline of the image-processing techniques incorporated to extract physical information from the DBI images: a) Detection of the extent of in-nozzle cavitation in the enlarged orifice and b) spray-cone angle measurement in the real-size layout. The spray cone-angle reported results as the addition of the half-angle formed between the major axis of each cyan ellipse and the horizontal. Animations of juxtaposed raw (panel i) and post-processed (panel iii) images corresponding to (a) have been provided as Supplementary Movie SM1. Likewise, animations of post-processed (panel iv) images corresponding to (b) for both enlarged and real-size layouts have been provided as Supplementary Movies SM2 and SM3, respectively. (For interpretation of the references to colour in this figure legend, the reader is referred to the web version of this article.)

detect the elongated cavities arising in the sac region.

The process to measure the spray cone-angle variation over time is shown in Fig. 6**b**. It must be noted that the method is universal and has been applied to measure the spray-cone angles in both the examined layouts. The first two steps remain the same as in the process to extract the cavity variation with time, i.e. background normalisation and binarisation. Subsequently, an edge detection algorithm (Sobel-Feldman operator) was applied to highlight the spray periphery. An ellipse was fitted to each identified spray edge and the orientation of the major axis of each ellipse was considered as the spray cone half angle. As the spray periphery, especially at sub-atmospheric ambient conditions, can become considerably perturbed a large extent of localised fluctuations it has been deemed that a spatially-averaged cone angle is reproduced in a more straightforward manner using the fitting in mention rather than point measurements at specific locations downstream the injector outlet. The last panel (iv) of Fig. 6**b** exhibits the fitted edges superimposed over the raw spray images and verifies the validity of the employed technique.

3. Results and discussion

In-cylinder pressure during operation of GDI engines can vary from deep vacuum up to a few bars depending on the engine load and the injection strategy followed. A range of 0.1–6.0 bar regarding the chamber pressure has been considered in this work as realistic ambient conditions. Four repetitions of each injection event were conducted to confirm results repeatability and to assess statistical error. Comparative results for the three fuel samples examined regarding cloud and vortical cavitation and spray-angle variation are presented in sections 3.1–3.3. Section 3.4 focuses on differences in the break-up behaviour between the Newtonian fuels (base, E10) and the viscoelastic blend.

3.1. *In-nozzle cavitation*

The temporally averaged presence probability of vapour within the enlarged orifice and corresponding standard deviation are plotted in Fig. 7. The contour plots were produced by averaging the vapour projected area identified at each time instance over the entire duration of

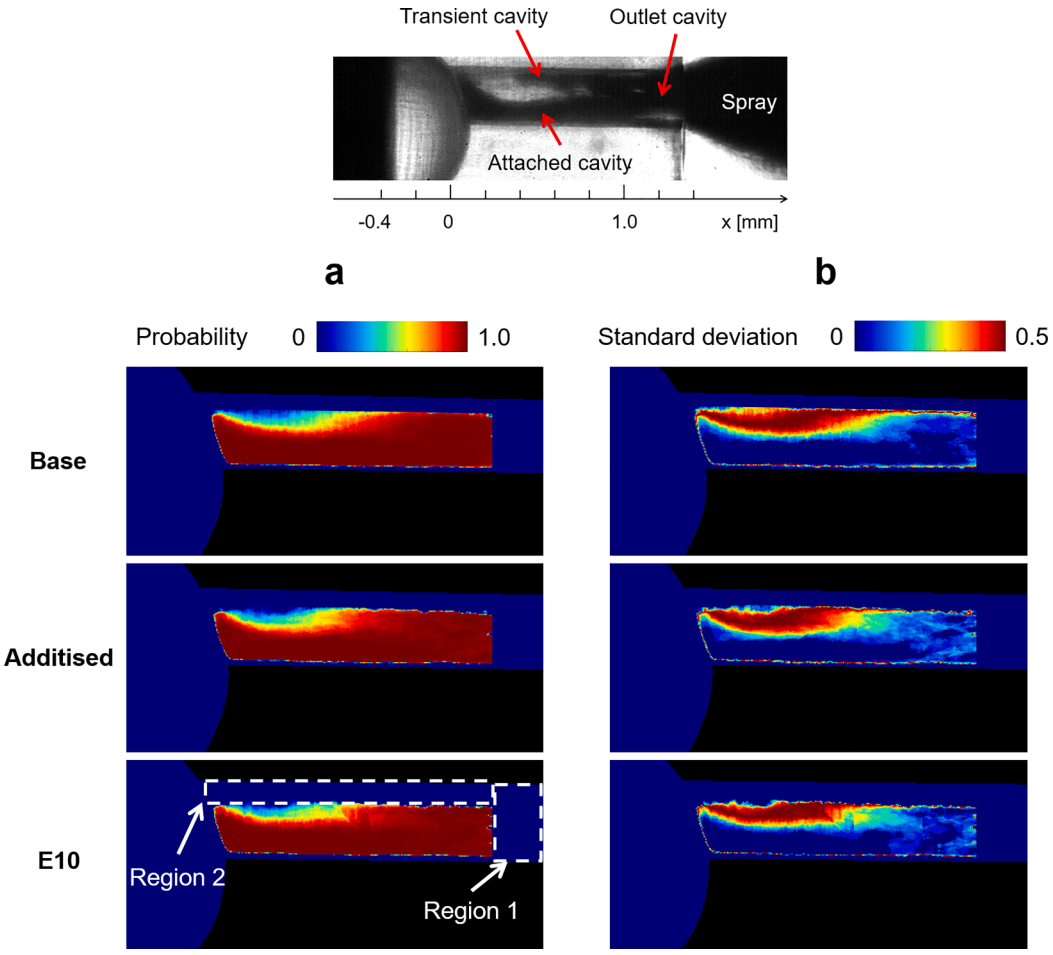

Fig. 7. Contour plots of in-nozzle a) vapour-presence probability and b) standard deviation at P_{amb} = 1.0 bar for the three fuels examined. Flow is from left to right. The inset depicts a time instance highlighting cavitation structures of characteristic morphology.

the injection event. For brevity, only the contour plots corresponding to ambient pressure of 1.0 bar are shown, since the relevant plots for the other ambient conditions examined are qualitatively similar. It should be noted that the last 0.2 mm prior to the nominal nozzle outlet, denoted as region 1 in Fig. 7**a**, have been masked out from image processing, since the refractive-index gradient stemming from in-nozzle cavitation could not be differentiated from the respective owing to spray formation. Likewise, the nozzle curvature close to the edge of the active window also obscured the clear identification of cavity outlines in the region and therefore 0.06 mm in the vicinity of the nozzle's upper projected edge, denoted as region 2 in Fig. 7**a**, have also been omitted from the analysis.

The well-established cavitation cloud forming at the lower part of the nozzle cross-section remained invariant during the injection event as reflected by the near-unity presence probability values (Fig. 7**a**) and respective absence of standard deviation (Fig. 7**b**). On the contrary, transient cavitating structures appeared on the upper part of the nozzle cross section extending roughly until the nozzle mid-length, as revealed by the high standard deviation values in the region. Past that location, transient structures merge with a static cavity forming at the nozzle

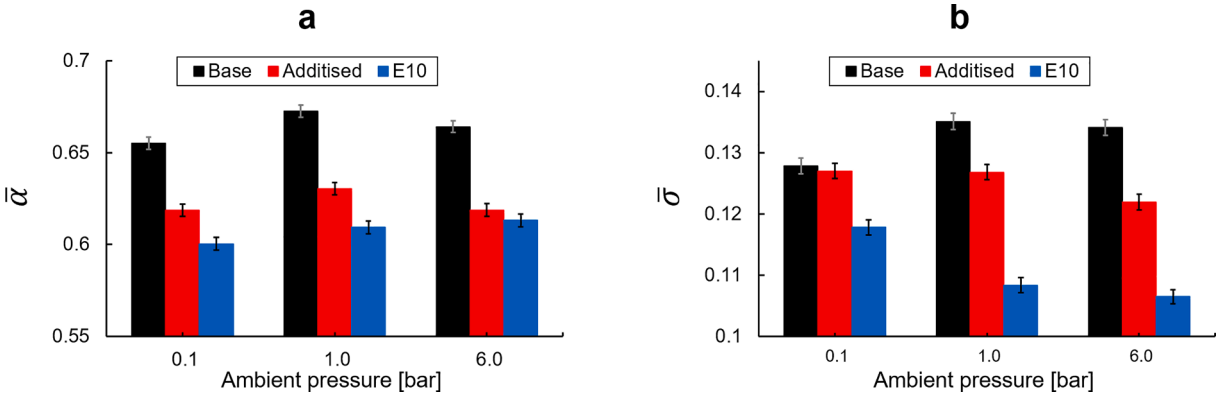

Fig. 8. Temporally and spatially averaged values of in-nozzle a) vapour-presence probability and b) standard deviation. Chart values have been calculated by spatially averaging the range of probability and standard deviation values in the nozzle area (excluding the final 0.2 mm of the nozzle exit).

outlet, as indicated by the moderate standard deviation values highlighting a level of flow unsteadiness in the region near the outlet. Although the underlying cause for the formation of cavitation at the outlet region is not completely clear, a moderate expansion of the nozzle hole, owing to the fabrication process, leading to cavitation onset has been observed in various types of optical tips.

Figure 8 provides a quantitative comparison of the probability of projected-vapour presence for the examined fuels and conditions. The bar charts were produced spatially averaging the presence-probability and standard-deviation values graphically shown in Fig. 7. Error bars correspond to standard statistical error ($=\pm\sigma/\sqrt{n}$), where n (=4) is the number of injection events conducted, and σ is the standard deviation of temporally and spatially averaged values. It is evident that the ambient pressure has a negligible effect on the presence-probability values for all fuels (Fig. 8**a**). This trend can be justified considering that the difference between the injection and ambient pressures leads to flow choking within the orifice in all cases, similar to what has been detected in real VCO gasoline injectors for much smaller pressure differences of the order of 10 bar [32,59]. It is also worth mentioning that the results shown here do not provide volumetric information of cavitation structures, therefore some uncertainty regarding overlapping cavitation structures along the line of sight does exist. Notwithstanding these facts, base gasoline exhibits measurably higher averaged presence-probability values compared to the additised and E10 blends. In all three ambient pressure conditions examined, the additised and E10 samples demonstrated on average 6% and 8% less cavitation probability compared to

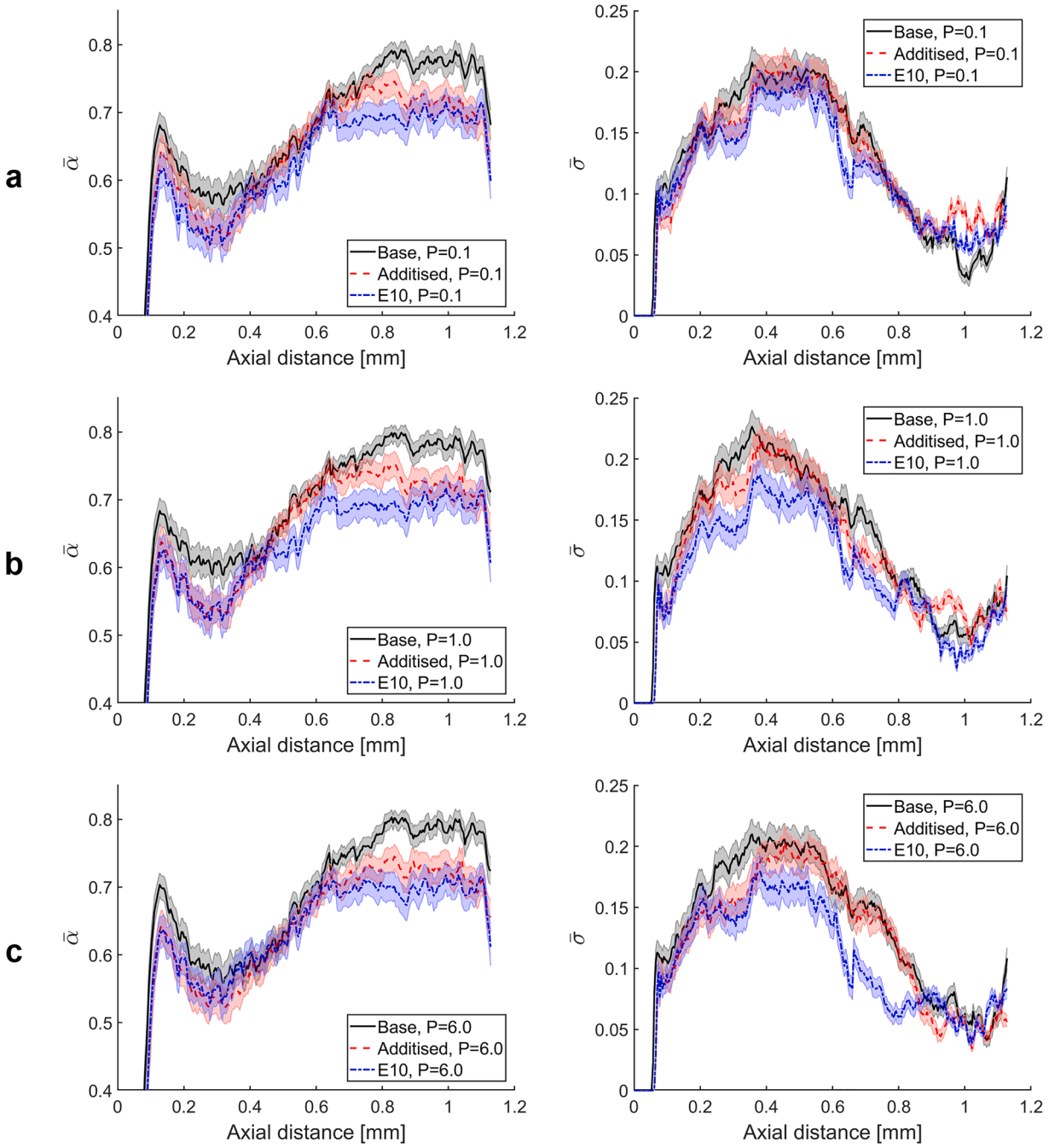

Fig. 9. Distribution of laterally-averaged vapour-presence probability and corresponding standard deviation along the orifice length: a) $P_{amb} = 0.1$ bar, b) $P_{amb} = 1.0$ bar, and c) $P_{amb} = 6.0$ bar. The shaded regions encompassing each line of same colour denote the standard statistical error ($= \pm\sigma/\sqrt{n}$), where the number of samples n (=65) corresponds to pixel values used for averaging per image column within the in-nozzle region.

base gasoline, respectively. The higher viscosity of the E10 leads to lower values of the local in-nozzle Reynolds number, which is expected to have a suppressive effect on cavitation onset. However, the differences between the base and additised fuels lower should be attributed exclusively to the influence of the fluid rheology.

Prior experiments of the authors' research group with reference to injector flows, nevertheless conducted with diesel fuels [47–49], have demonstrated that viscoelasticity induced by the presence of QAS tends to suppress cloud (or geometric) cavitation. A similar influence is plausible for gasoline fuels as well. The underlying cause is the interaction of flexible polymeric chains, forming due to the presence of the additive, with large-scale cross-flow vortices that leads to damping of their coherence. Certainly, it has also been well established in the literature [60,61] that viscoelasticity disrupts the turbulence energy cascade to smaller scales, thus leading to a reduction of the overall level of turbulence.

The standard-deviation results depicted in Fig. 8**b** also show decreased values for the additised and E10 samples compared to the base gasoline. This trend complies with the arguments stated above regarding cavitation suppression. Regarding E10, increased temporal flow stability is linked with the increased fuel viscosity, while the turbulence-reducing effect of viscoelastic additives has a causal connection with flow stabilisation, although they could also facilitate the prevalence of elongated cavities [49].

In order to further pinpoint differences between the examined fuels in the enlarged orifice, laterally averaged values of vapour presence and their corresponding standard-deviation values with respect to nozzle axial distance are provided in Fig. 9. In other words, the values at each axial location were acquired by averaging the values of each column of pixel values shown in Fig. 7. As can be seen in Fig. 7**a,** base gasoline exhibits the highest vapour-presence probability at the orifice part closer to the outlet (axial distance higher than 0.6 mm), where the most significant cavitation extent is observed, refer to the inset of Fig. 7. The trend appears to be consistent regardless of the ambient pressure. A more moderate suppressive trend in the vapour-presence probability for the additised and E10 samples can also be discerned for axial distances between 0.1 and 0.4 mm, i.e., at the location of the attached cloud cavity. Moreover, the standard deviation plots of Fig. 7**b** demonstrate that the E10 sample shows a clear tendency to stabilise the cavitating flow compared to the other fuels, with the differences being more pronounced for $P_{amb} \geq 1$ bar. The trend should be attributed to the damping of flow perturbations, owing to the higher fuel viscosity. For the same ambient-pressure range, the additised fuel exhibits moderately smaller standard-deviation values compared to the base gasoline, for axial locations below 0.4 mm. It seems that the turbulence-reducing effect of viscoelasticity leads to a more stable attached cloud cavity in the case of the additised sample.

3.2. Vortical cavitation in the sac volume

Cavities of elongated shape have been established to emerge in fuel injectors due to the underlying action of longitudinal vortices; such structures have been conventionally referred to as string cavities [62]. As can be discerned in the top-view images of Fig. 5**b**, slender cavities with short lifespans are detected in the sac region of the enlarged orifice and are subsequently entrained into the nozzle hole. With the same rationale as Fig. 7, the temporally-averaged presence probability and standard deviation of vortical cavitation in the hemispherical sac is depicted in Fig. 10. For brevity, only the plots for $P_{amb} = 1.0$ bar are presented, since a qualitatively similar trend has been verified regardless of the ambient pressure. The low probability (Fig. 10**a**) and high standard deviation (Fig. 10**b**) values denote the highly transient nature of vortical cavities. The underlying vortices emanate either from the needle tip or the gap between the needle and needle seat, while filament roll-up is also facilitated by the significant curvature of the sac wall. The probability peaks at the nozzle entrance region suggest that the majority

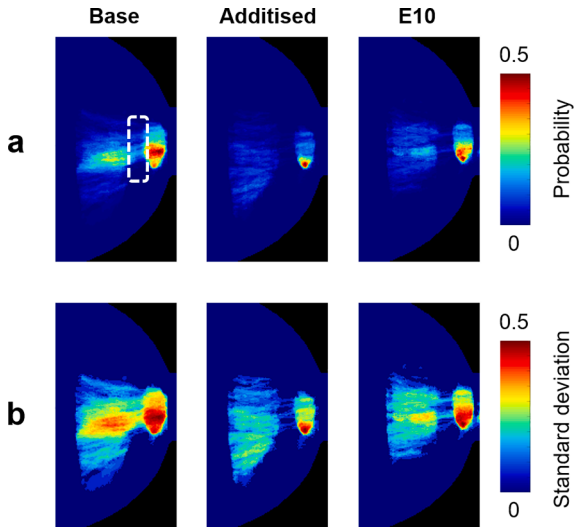

Fig. 10. Contour plots of vortical cavity a) presence probability and b) standard deviation in the sac region of the enlarged-orifice tip for $P_{amb} = 1.0$ bar. A discontinuity in the structures' topology can be seen in the plots as in the location of the entrance hole (white dashed lines) where measurable signal could not be extracted. Flow is from left to right.

of string cavities are eventually entrained into the nozzle and contribute to the transient features highlighted by the contour plot of Fig. 7.

A quantitative comparison between the examined fuel samples in terms of spatially averaged, within the entire sac region, presence-probability, and standard-deviation values at different flow conditions are available in Fig. 11. It should be noted that since cavity size is much smaller than the sac area and vapour is mostly absent from the sac volume throughout the injection, the spatially averaged probability (Fig. 11**a**) obtains low values, in the range of 0.7%–1.9%. Measurable differences can be discerned for $P_{amb} = 0.1$ and 1 bar, with the base fuel obtaining higher presence-probability and standard-deviation values than the additised and E10 samples. The highly fluctuating nature and moderate appearance frequency of vortical cavities contribute to the statistical error. However, the arguments reported in the discussion relevant to in-nozzle cavitation, i.e., that its extent and flow instabilities in general, as suggested by higher standard-deviation values (Fig. 11**b**), which are more pronounced for the base sample, seem to be supported by the results referring to vortical cavitation as well.

It should be clarified here that previous works referring to diesel injection in enlarged orifices have demonstrated that in-nozzle vortical cavitation was enhanced in the presence of viscoelastic additives [47–49]. The proposed mechanism correlated the enhancement of the underlying vortex coherence with the reduction of the overall level of turbulence, i.e., vortices within the nozzle at smaller scales, which would tend to dissipate the energy of large-scale longitudinal vortices. Unlike the aforementioned experiments, longitudinal vortices never accomplish a stable behaviour, yet retain their coherence for only a few μs in the present experiments, owing also to flow instabilities induced by the transient needle motion. It can therefore be postulated that more extensive vortex roll-up occurs due to a more perturbed flow for the base fuel, an argument in alignment with the discussion outlined regarding in-nozzle cloud cavitation (refer to Figs. 7-8).

An additional comment should be made regarding the behaviour of the examined samples behaviour for an ambient pressure of 6 bar, where noticeable differences seem to decay. The elevated ambient pressure certainly reduces the in-nozzle Reynolds number and potentially slightly influences hydraulic characteristics on the injection, such as the needle wobble. As a consequence, the flow seems to be stabilised overall, leading to few occurrences of vortical cavities in the sac.

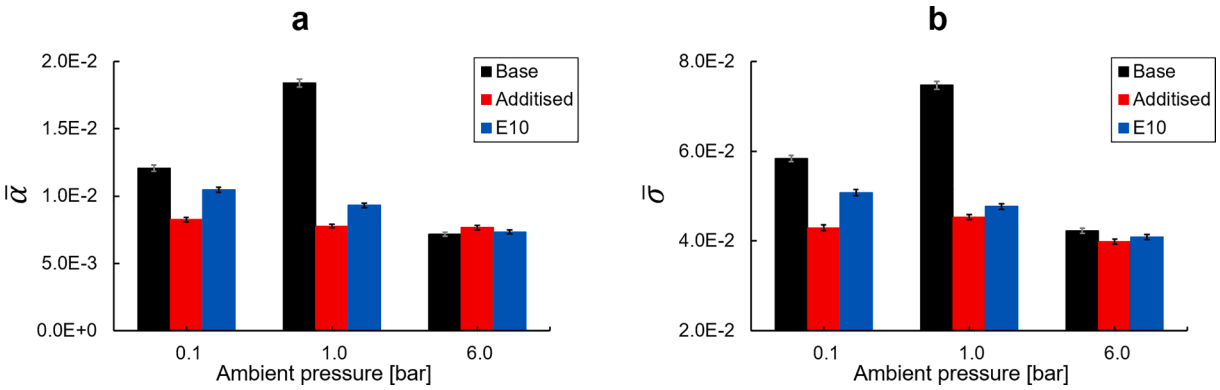

Fig. 11. Temporally and spatially averaged values of vortical cavitation: a) presence probability and b) standard deviation. Graphs values have been calculated by spatially averaging the probability and standard-deviation values obtained in the sac region, which are graphically depicted in the contour plots of Fig. 10.

3.3. Spray cone angle

Four repetitions of an injection event were analysed for each ambient pressure examined to quantify the spray-cone angle temporal variation and satisfactory repeatability was confirmed for both injector layouts even for the extreme case of deep vacuum. Fig. 12, indicatively depicts the cone angle distribution with time for the base gasoline at the downstream of both the enlarged (Fig. 12**a**) and real-size injector tips (Fig. 12**b–d**), with the statistical error represented as shaded bands. Time values in the horizontal axis of Fig. 12, are presented in a non-dimensional form as $t^* = t/t_{tot}$, as the total injection duration (t_{tot}) differs slightly depending on the optical tip and the ambient pressure. Common trends can be detected for both tips, in the sense that the cone-angle absolute values increase as the ambient pressure decreases from atmospheric to vacuum, owing to the explosive atomisation of bubbles induced by the extreme ratio of back to injection pressure. Increasing of the ambient pressure to 6.0 bar lead to an increase in the absolute cone-angle values only for the two-hole tip, while the opposite trend was observed for the enlarged orifice. For a pressurised environment, any influence on the cone angle stems from aerodynamic rather than phase-

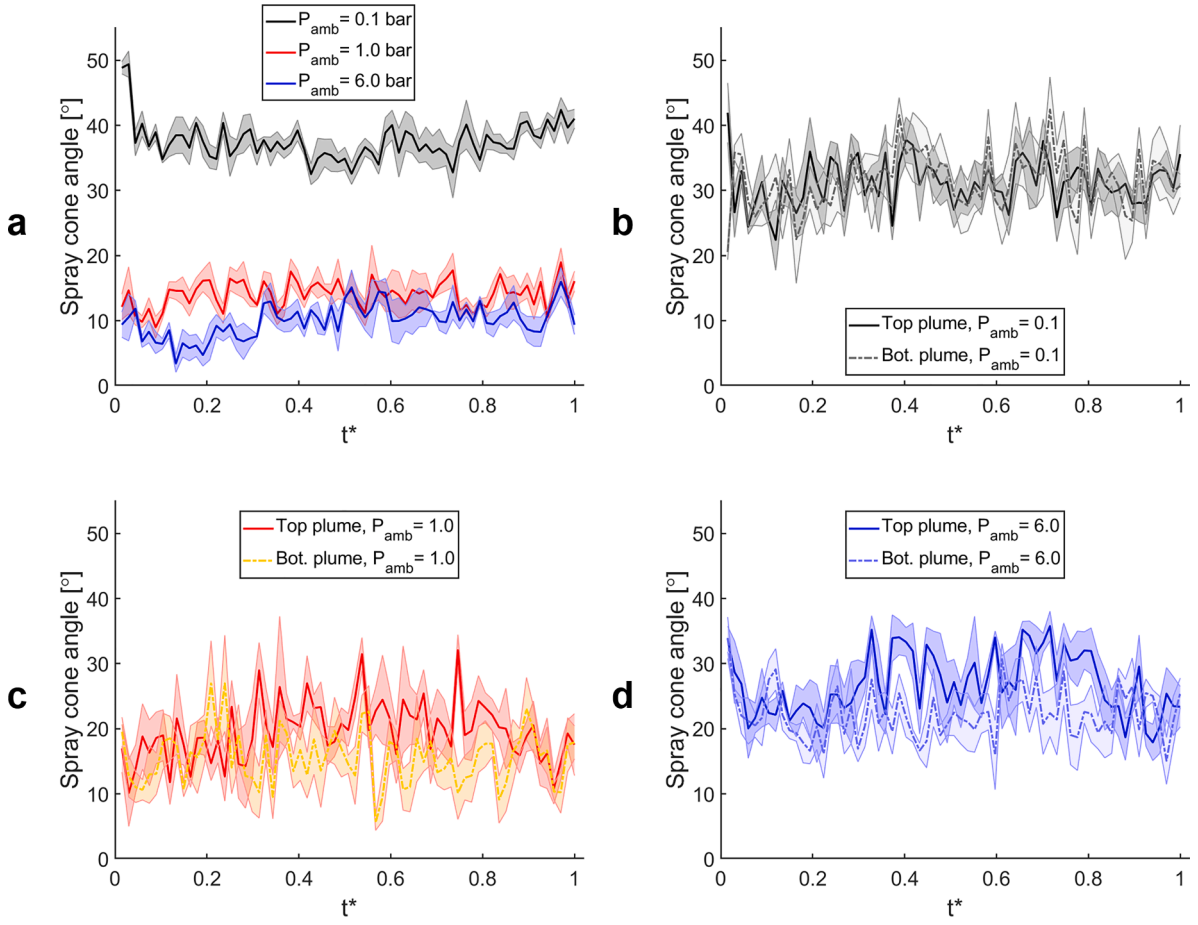

Fig. 12. Spray cone-angle distribution with time for base gasoline at different ambient pressures: a) enlarged-orifice and two-hole layout b) P_{amb} = 0.1 bar, c) P_{amb} = 1.0 bar, d) P_{amb} = 6.0 bar. Top and bottom plumes refer to the tip orientation as depicted in Fig. 5**c**. The shaded regions encompassing each line of same colour denote the standard statistical error.

change phenomena and therefore the increased values for the real-size injector have to be attributed to increased drag forces acting on the spray plume. A similar effect is nonetheless absent for the enlarged orifice since the minimum cone-angle values are observed for P_{amb} = 6.0 bar. It is postulated that the considerable jet momentum owing to the large orifice cross section prevents primary aerodynamic break-up.

As the real-size tip realises two nozzle-holes, cone-angle measurements are presented separately in Fig. 12**b–d** for different ambient pressures. A systematic difference, yet on the verge of measuring capability, in the cone angle values of the two plumes was observed for all fuels for P_{amb} = 1.0–6.0 bar. This discrepancy mainly emanates flow processes taking place in the internal flow path of the tip, and namely in asymmetries in the secondary flow pattern establishing in the sac and nozzle regions and in the topology of in-nozzle cavitation. The shape fidelity of the counterbore holes could also influence the spray plume extent.

Temporally averaged plume-angle values for each fuel and condition examined are presented in Fig. 13. Referring to the results for the two-hole injector, the average of both plumes is presented in the bar charts of Fig. 13**b**. With regards to the fuel types examined, insignificant differences were observed for ambient pressures of 1.0 and 6.0 bar conditions, where break-up is controlled by aerodynamic processes. This finding is expected for cold fuels and is in agreement with previous experimental studies focusing on spray break up of gasoline and ethanol blends [63]. On the other hand, at vacuum conditions where effervescent atomisation sets in [64,65], both additised and E10 blends showed measurably higher plume angles compared to base in both layouts. The main reason behind higher plume angles for E10 should be sought to its thermodynamic properties and, more specifically, to the increased vapour pressure and volatility compared to the base [55], as also suggested by the distillation curves of Fig. 3. The justification for the behaviour of the additised fuel should be pursued in its rheological characteristics and primarily to their effect on the in-nozzle two-phase flow field. The reduced cavitation extent and overall flow stabilisation observed for the additised sample lead to increased flowrate though the injector. Since spray topology and dynamics are highly influenced by the in-nozzle flow conditions or in other words the local Weber number in the near-nozzle region is expected to be higher for the additised sample, which consequently affects primary breakup and plume angle.

3.4. Spray and ligament break-up

The spray break-up characteristics for each fuel sample were further investigated by deriving 'lumped' metrics of the number of satellite droplets detaching from the main plume. Due to limitations imposed by the spatial and temporal resolution, the peripheries of discrete structures could not be clearly identified. However, in order to evaluate the extent at which fine structures or droplets detach from the main fuel jet, the averaged pixel brightness of the region surrounding the liquid core of the spray was selected as a representative measure of the fuel jet propensity for primary breakup.

Following the edge detection and binarisation techniques outlined in section 2.2, the intact liquid core of the fuel jet expelled by the injector was detected dynamically in each frame and removed from the raw image, as shown in the first frames of Fig. 14**a-b**. As a result of image subtraction from background images where the fuel spray was absent, brighter pixels correspond to detached liquid structures, as illustrated by the second frames of Fig. 14**a-b**. Furthermore, the brightness level was normalised so that values of zero and one correspond to black and white pixels, respectively.

Figure 14**c and d** present a quantitative comparison of the averaged brightness at the jet periphery for the examined fuel samples. Results only for the ambient pressures of 0.1 bar and 6.0 bar are presented, since satellite structures were observed only for those. In fact, especially for 6.0 bar aerodynamic break-up was observed only for the two-hole nozzle (Fig. 14**d**), yet values are presented for both layouts for completeness purposes. Fig. 14**c** referring to the enlarged orifice, illustrates that for P_{amb} = 0.1 bar, the additised and E10 samples showed approximately 15% higher mean brightness compared to base, denoting the presence of more satellite structures and confirming the capability of the samples to induce finer spray atomisation, as inferred in the discussion regarding the spray-cone angle relevant to Fig. 13. For ambient pressure of 6.0 bar in the specific geometry, the differences in the mean brightness were negligible, which once again, should be sought in the inertial nature of break up and the relatively low local flow velocity owing to the large nozzle cross section.

Concerning the real-size injector tip (Fig. 14**d**) in vacuum ambient conditions, additised and E10 blends showed average brightness 14% and 22% higher than base. The presence of counterbores in this layout appears to reinforce the break-up process at pressurised ambient. The additised and E10 samples exhibited slightly yet measurably higher average-brightness values, demonstrating once again their proneness to break-up. Once more, enhanced spray breakup in the additised blend is owed to its rheological characteristics also influencing the in-nozzle two-phase flow field as previously discussed. Referring to E10, enhanced atomisation emanates from the increased fuel volatility.

For a pressurised environment, once the needle reaches its lowest point, residual fuel in the internal flow path of the injector is expelled in the chamber in the form of ligaments and large droplets [66–68]. As these liquid structures have low ejection velocities and considerable sizes, small evaporation rates increase the combustion time scale, which contributes to additional engine soot [69]. In the present campaign, characteristic post injection ligaments were observed in the two-hole tip for P_{amb} = 6.0 bar, refer to the upper panel of Fig. 15**a**. As the nozzle volume was much larger in the enlarged tip, a higher fuel quantity was expelled after end of injection in the form of coalescing ligaments and,

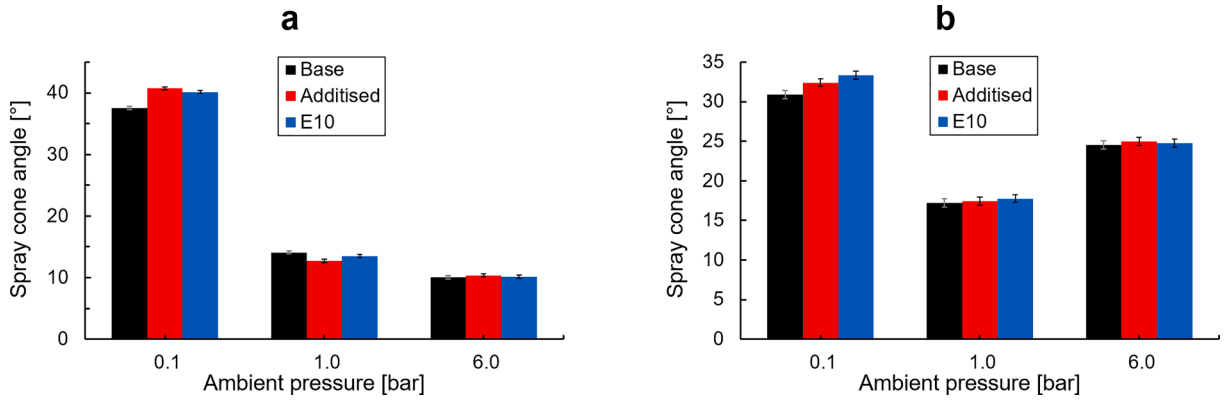

Fig. 13. Temporally-averaged spray cone-angle in a) the enlarged orifice and b) two-hole layout. The mean values and error bars have been calculated from four injection cycles at each condition.

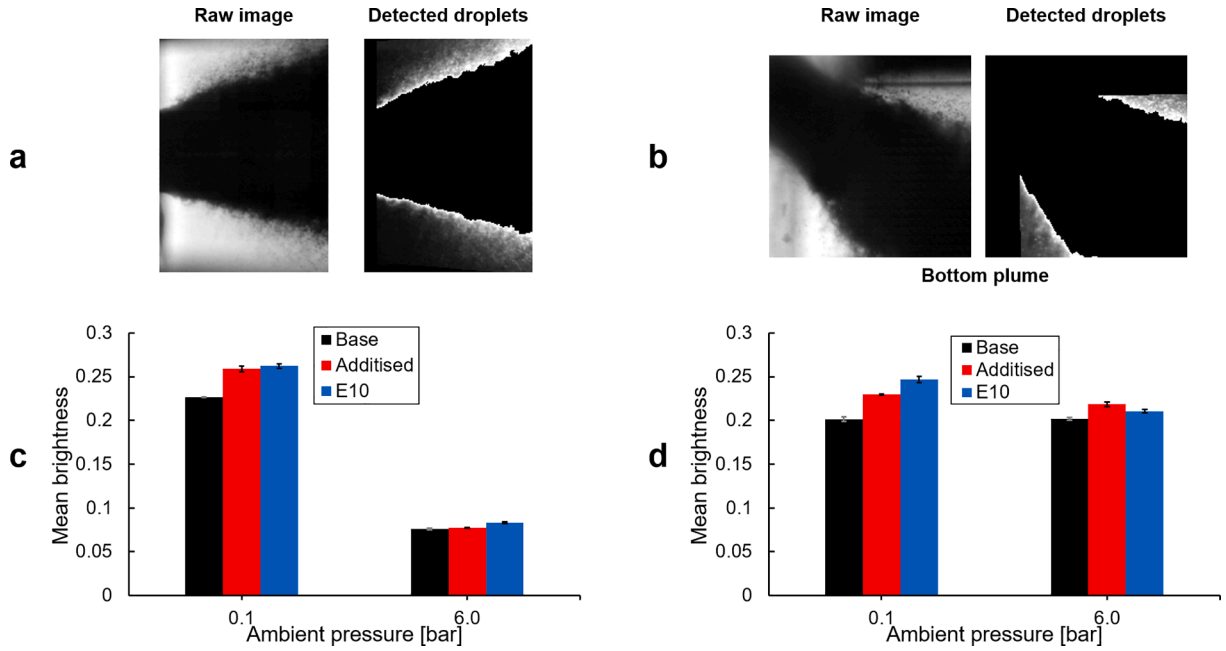

Fig. 14. a) Highlighted satellite structures in the enlarged-orifice and b) two-hole layouts. c) Mean brightness of satellite structures in enlarged orifice and d) real-size, two-hole layout. The brightness values were averaged for both plumes of the real-size tip.

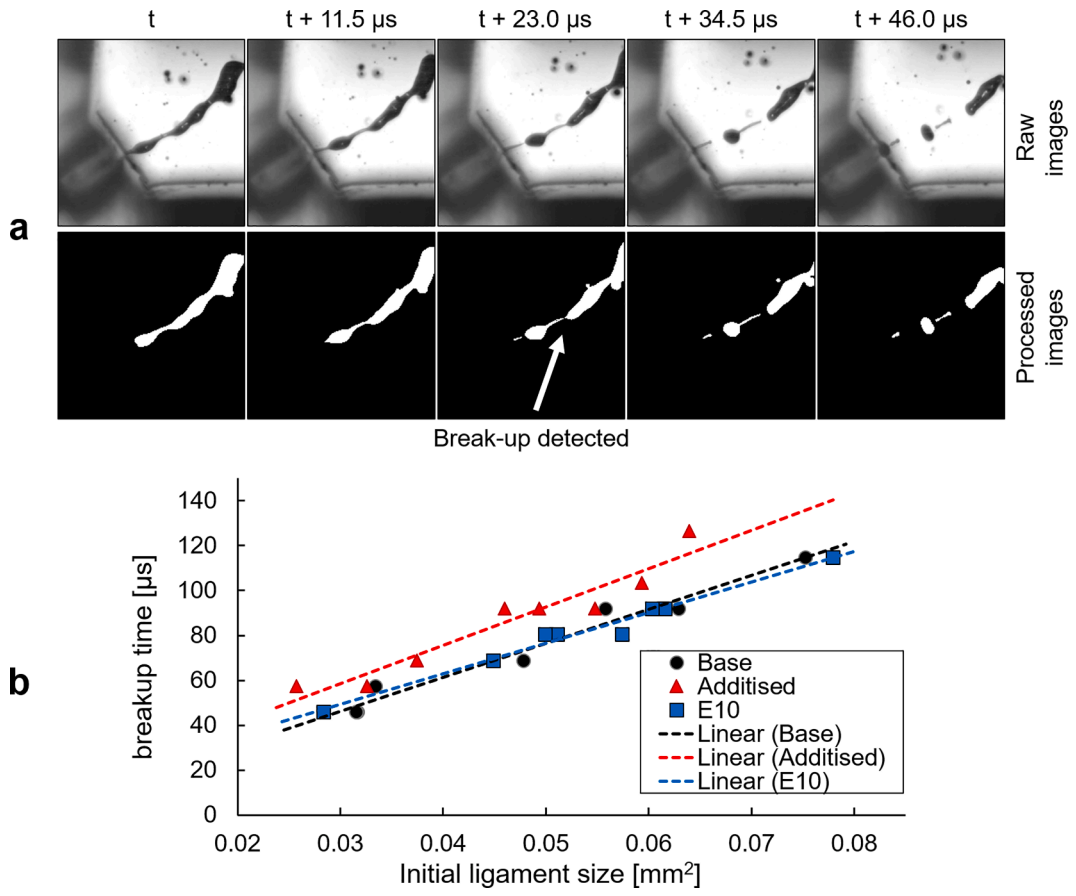

Fig. 15. a) Temporal evolution of ligament breakup and corresponding processed images after the end of injection in the top plume of the real-size model. Time interval between consecutive images is 11.5 μs. b) Ligament breakup time over initial size of ligament projected area in real size injector tip at P_{amb} = 6.0 bar.

thus, discrete structures could not be identified and processed. On the contrary, a frothy two-phase mixture formed downstream the injector outlet for lower ambient pressures due to extensive bubble coalescence.

The size and breakup time of the detected ligaments, as annotated in Fig. 15**a** were recorded for the examined samples and are presented in correlation in Fig. 15**b**. It is clear that the additised sample shows higher

breakup times for the range of ligament sizes identified, while base gasoline and E10 exhibit an indistinguishable behaviour.

Fundamental studies on liquid jet instabilities have shown that viscoelastic liquids tend to exhibit a 'beads-on-a-string topology' liquid-filament topology [70] and increased break-up lengths compared to Newtonian counterparts. This distinct behaviour has been correlated to the fluid extensional rheology and more specifically to the extensional relaxation time representative of the fluid elasticity [71]. It appears that for post-injection droplet dynamics, such rheological effects, macroscopically perceived as increase of elongational viscosity, are significant for the additised sample. Albeit this behaviour seems to be counterintuitive, given the fact that the additised sample exhibits a higher propensity for spray break-up, it must be taken into account that flow velocities or in other words the local Weber number is much higher during injection and its effect is dominant in designating the break-up behaviour. It has been summarised in [71] that a number of competing factors designate the indicative droplet sizes after break up of non-Newtonian liquid jets, reflected in the Weber, Ohnesorge, and Deborah numbers.

4. Conclusions

High-speed DBI performed in a real-size two-hole and an enlarged single-hole optical injector illustrated the differences in terms of in-nozzle cavitation and near-nozzle spray morphology of conventional and alternative gasoline fuel types. The behaviour of a standardised gasoline was comparatively assessed against an E10 blend representative of widely-employed renewable fuels and a gasoline blend additised with QAS viscoelasticity inducing agents. For the examined conditions the additised and E10 samples demonstrated on average 6% and 8% less extent of cavitation in the enlarged orifice compared to the base gasoline, respectively. In addition, both samples were associated with temporally stabilised internal flow compared to reference. In terms of spray atomisation and dynamics, once again, the behaviour of the additised sample was found to resemble that of E10, characterised by increased cone angles and propensity for break-up in sub-atmospheric pressure conditions, as 15% more satellite droplets in the spray periphery were detected compared to base. Albeit E10 and additised blends exhibit a macroscopically similar flow behaviour the underlying causes are different and should be associated with the thermodynamic and transport properties of the former, whereas only with the distinct rheology of the latter. The distinct rheology of the additised sample is also responsible for the differences in the break-up behaviour of liquid ligaments expelled by the nozzles of the two-hole tip after the end of injection. To summarise, the enhancement of spray atomisation through addition of QAS additives to gasoline was demonstrated in this work. Furthermore, blending of such additives in commercial gasoline, is not associated with unattractive features of ethanol-blended fuel, such as reduced heating value resulting to reduced power output and fuel efficiency.

CRediT authorship contribution statement

Milad Heidari-Koochi: Software, Validation, Formal analysis, Data curation, Writing – original draft, Visualization. **Ioannis K. Karathanassis:** Conceptualization, Methodology, Software, Validation, Formal analysis, Investigation, Data curation, Writing – review & editing, Visualization, Supervision, Project administration, Funding acquisition. **Phoevos Koukouvinis:** Software, Validation, Formal analysis, Investigation, Project administration, Funding acquisition. **Joonsik Hwang:** Validation, Investigation, Resources. **Lyle M. Pickett:** Conceptualization, Investigation, Resources, Supervision, Project administration, Funding acquisition. **David Spivey:** Investigation, Resources. **Manolis Gavaises:** Visualization, Supervision, Funding acquisition.

Declaration of Competing Interest

David Spivey is a full time employee of the Lubrizol Corporation. All other authors declare that they have no known competing financial interests or personal relationships that could have appeared to influence the work reported in this paper.

Acknowledgements

The work was performed at the Combustion Research Facility (CRF), Sandia National Laboratories, Livermore, CA. Sandia National Laboratories is a multi-mission laboratory managed and operated by National Technology and Engineering Solutions of Sandia, LLC., a wholly owned subsidiary of Honeywell International, Inc., for the U.S. Department of Energy's National Nuclear Security Administration under contract DE-NA0003525. Funding from the EU Horizon-2020 Marie Skłodowska-Curie Global Fellowships AHEAD (IK, Grant No. 794831) and UNIFIED (PK, Grant No. 748784) is acknowledged, which also supported the international visiting program of Ioannis K. Karathanassis and Phoevos Koukouvinis at the Sandia National Laboratories. Additional funding has been received by the UK's Engineering and Physical Sciences Research Council (EPSRC) through grant EP/K020846/1.

Appendix A. Supplementary data

Supplementary data to this article can be found online at https://doi.org/10.1016/j.enconman.2021.115109.

References

[1] "BNEF EVO Report 2020 | BloombergNEF | Bloomberg Finance LP" [Online]. Available: https://about.bnef.com/electric-vehicle-outlook/. [Accessed: 26-May-2021].
[2] Quintero JA, Montoya MI, Sánchez OJ, Giraldo OH, Cardona CA. Fuel ethanol production from sugarcane and corn: comparative analysis for a colombian case. Energy 2008;33(3):385–99. https://doi.org/10.1016/j.energy.2007.10.001.
[3] Pimentel D, Patzek TW. Ethanol production using corn, switchgrass, and wood; biodiesel production using soybean and sunflower. Nat Resour Res 2005;14(1):65–76. https://doi.org/10.1007/s11053-005-4679-8.
[4] Mielenz JR. Ethanol production from biomass: technology and commercialization status. Curr Opin Microbiol 2001;4(3):324–9. https://doi.org/10.1016/S1369-5274(00)00211-3.
[5] Bayraktar H. Experimental and theoretical investigation of using gasoline-ethanol blends in spark-ignition engines. Renew Energy 2005;30(11):1733–47. https://doi.org/10.1016/j.renene.2005.01.006.
[6] Yüksel F, Yüksel B. The use of ethanol-gasoline blend as a fuel in an SI engine. Renew Energy 2004;29(7):1181–91. https://doi.org/10.1016/j.renene.2003.11.012.
[7] Costa RC, Sodré JR. Hydrous ethanol vs. gasoline-ethanol blend: engine performance and emissions. Fuel 2010;89(2):287–93. https://doi.org/10.1016/j.fuel.2009.06.017.
[8] Aleiferis PG, Serras-Pereira J, Augoye A, Davies TJ, Cracknell RF, Richardson D. Effect of fuel temperature on in-nozzle cavitation and spray formation of liquid hydrocarbons and alcohols from a real-size optical injector for direct-injection spark-ignition engines. Int J Heat Mass Transf 2010;53(21):4588–606. https://doi.org/10.1016/j.ijheatmasstransfer.2010.06.033.
[9] Aleiferis P, Romunde ZV. An analysis of spray development with Iso-Octane, n-Pentane, Gasoline, Ethanol and n-Butanol from a multi-hole injector under hot fuel conditions. Fuel 2013;105:143–68. https://doi.org/10.1016/j.fuel.2012.07.044.
[10] Baecker H, Kaufmann A, Tichy M. Experimental and simulative investigation on stratification potential of spray-guided GDI combustion systems. *SAE Technical Papers*, SAE International. 2007. https://doi.org/10.4271/2007-01-1407.
[11] Lu X, Han D, Huang Z. Fuel design and management for the control of advanced compression-ignition combustion modes. Prog Energy Combust Sci 2011;37(6):741–83. https://doi.org/10.1016/j.pecs.2011.03.003.
[12] Montanaro A, Malaguti S, Alfuso S. Wall impingement process of a multi-hole GDI spray: experimental and numerical investigation. *SAE Technical Papers*, SAE International 2012. https://doi.org/10.4271/2012-01-1266.
[13] Costa M, Sorge U, Allocca L. Increasing energy efficiency of a gasoline direct injection engine through optimal synchronization of single or double injection strategies. Energy Convers Manag 2012;60:77–86. https://doi.org/10.1016/J.ENCONMAN.2011.12.025.
[14] Saliba G, Saleh R, Zhao Y, Presto AA, Lambe AT, Frodin B, et al. Comparison of Gasoline Direct-Injection (GDI) and Port Fuel Injection (PFI) vehicle emissions: emission certification standards, cold-start, secondary organic aerosol formation potential, and potential climate impacts. Environ Sci Technol 2017;51(11):6542–52. https://doi.org/10.1021/acs.est.6b06509.

[15] Zhu R, Hu J, Bao X, He L, Lai Y, Zu L, et al. Tailpipe emissions from gasoline direct injection (GDI) and port fuel injection (PFI) Vehicles at both low and high ambient temperatures. Environ Pollut 2016;216:223–34. https://doi.org/10.1016/j.envpol.2016.05.066.

[16] Salvador FJ, Carreres M, Jaramillo D, Martínez-López J. Comparison of microsac and VCO diesel injector nozzles in terms of internal nozzle flow characteristics. Energy Convers Manag 2015;103:284–99. https://doi.org/10.1016/J.ENCONMAN.2015.05.062.

[17] Befrui B, Corbinelli G, D'Onofrio M, Varble D. GDI Multi-Hole Injector Internal Flow and Spray Analysis. In: SAE 2011 World Congress and Exhibition; 2011. https://doi.org/10.4271/2011-01-1211.

[18] Skogsberg M, Dahlander P, Denbratt I. Spray shape and atomization quality of an outward-opening piezo gasoline Di injector. *SAE Technical Papers*, SAE International. 2007. https://doi.org/10.4271/2007-01-1409.

[19] Schulz F, Schmidt J, Kufferath A, Samenfink W. Gasoline wall films and spray/wall interaction analyzed by infrared thermography. SAE Int J Engines 2014;7(3):1165–77. https://doi.org/10.4271/2014-01-1446.

[20] Chaves H, Knapp M, Kubitzek A, Obermeier F, Schneider T. Experimental study of cavitation in the nozzle hole of diesel injectors using transparent nozzles. SAE Trans 1995;104:645–57. https://doi.org/10.4271/950290.

[21] He Z, Zhang Z, Guo G, Wang Q, Leng X, Sun S. Visual experiment of transient cavitating flow characteristics in the real-size diesel injector nozzle. Int. Commun. Heat Mass Transf. 2016;78:13–20. https://doi.org/10.1016/j.icheatmasstransfer.2016.08.004.

[22] Nouri JM, Mitroglou N, Yan Y, Arcoumanis C. Internal flow and cavitation in a multi-hole injector for gasoline direct-injection engines. *SAE Technical Papers*, SAE International. 2007. https://doi.org/10.4271/2007-01-1405.

[23] Gavaises M, Papoulias D, Andriotis A, Giannadakis E, Theodorakakos A. Link between cavitation development and erosion damage in diesel injector nozzles. SAE Tech. Pap. 2007;01:0246. https://doi.org/10.4271/2007-01-0246.

[24] Koukouvinis P, Gavaises M, Li J, Wang L. Large eddy simulation of diesel injector including cavitation effects and correlation to erosion damage. Fuel 2016;175:26–39. https://doi.org/10.1016/j.fuel.2016.02.037.

[25] Koukouvinis P, Karathanassis IK, Gavaises M. Prediction of cavitation and induced erosion inside a high-pressure fuel pump. Int J Engine Res 2018;19(3):360–73. https://doi.org/10.1177/1468087417708137.

[26] Javier López J, Salvador FJ, De La Garza OA, Arrègle J. A comprehensive study on the effect of cavitation on injection velocity in diesel nozzles. Energy Convers Manag 2012;64:415–23. https://doi.org/10.1016/j.enconman.2012.03.032.

[27] Schmidt DP, Corradini ML. The internal flow of diesel fuel injector nozzles: a review. Int J Engine Res 2001;2(1):1–22. https://doi.org/10.1243/1468087011545316.

[28] Serras-Pereira J, van Romunde Z, Aleiferis PG, Richardson D, Wallace S, Cracknell RF. Cavitation, primary break-up and flash boiling of gasoline, Iso-Octane and n-pentane with a real-size optical direct-injection nozzle. Fuel 2010;89(9):2592–607. https://doi.org/10.1016/j.fuel.2010.03.030.

[29] Arcoumanis C, Badami M, Flora H, Gavaises M. Cavitation in real-size multi-hole diesel injector nozzles. SAE Trans 2000:1485–500. https://doi.org/10.4271/2000-01-1249.

[30] Roth H, Gavaises M, Arcoumanis C. Cavitation initiation, its development and link with flow turbulence in diesel injector nozzles. SAE Trans 2002;111:561–80. https://doi.org/10.4271/2002-01-0214.

[31] Mitroglou N, Gavaises M, Nouri J, "Cavitation inside Enlarged and Real-Size Fully Transparent Injector Nozzles and Its Effect on near Nozzle Spray Formation," *DIPSI Workshop 2011. Droplet Impact Phenomena & Spray Investigations*, pp. 33–45. 2011.

[32] Gilles-Birth I, Rechs M, Spicher U, Bernhardt S. Experimental investigation of the in-nozzle flow of valve covered orifice nozzles for gasoline direct injection. Proc 7th Int Symp Intern Combust Diagnostics 2006:59–78.

[33] Jiang G, Zhang Y, Wen H, Xiao G. Study of the generated density of cavitation inside diesel nozzle using different fuels and nozzles. Energy Convers Manag 2015;103:208–17. https://doi.org/10.1016/j.enconman.2015.06.065.

[34] Mamaikin D, Knorsch T, Rogler P, Wensing M. Experimental investigation of flow field and string cavitation inside a transparent real-size GDI nozzle. Exp Fluids 2020;61(7):154. https://doi.org/10.1007/s00348-020-02982-y.

[35] Hwang J, Yasutomi K, Arienti M, Pickett LM. Numerical investigation of near nozzle flash-boiling spray in an axial-hole transparent nozzle. *SAE Technical Papers*, SAE International 2020. https://doi.org/10.4271/2020-01-0828.

[36] Huang Y, Huang S, Huang R, Hong G. Spray and evaporation characteristics of ethanol and gasoline direct injection in non-evaporating, transition and flash-boiling conditions. Energy Convers Manag. 2016;108:68–77. https://doi.org/10.1016/J.ENCONMAN.2015.10.081.

[37] Mohammed MK, Balla HH, Al-Dulaimi ZMH, Kareem ZS, Al-Zuhairy MS. Effect of ethanol-gasoline blends on SI engine performance and emissions. Case Stud Therm Eng 2021;25:100891. https://doi.org/10.1016/j.csite.2021.100891.

[38] Iodice P, Senatore A, Langella G, Amoresano A. Effect of ethanol-gasoline blends on CO and HC emissions in last generation SI engines within the cold-start transient: an experimental investigation. Appl Energy 2016;179:182–90. https://doi.org/10.1016/j.apenergy.2016.06.144.

[39] Christie MJ, Fortino N, Yilmaz H. Parameter optimization of a turbo charged direct injection flex fuel SI engine. SAE Technical Papers, SAE International 2009;2(1):123–33. https://doi.org/10.4271/2009-01-0238.

[40] Kheiralla AF, El-Awad M, Hassan MY, Hussen MA, Osman HI. Effect of ethanol-gasoline blends on fuel properties characteristics of spark ignition engines. Univ Khartoum Eng J 2011;1(2):22–8.

[41] Bennett J. Advanced Fuel additives for modern internal combustion engines. Altern Fuels Adv Veh Technol Improv Environ Perform Towar Zero Carbon Transp 2014:165–94. https://doi.org/10.1533/9780857097422.1.165.

[42] Aradi AA, Colucci WJ, Scull HM, Openshaw MJ. A study of fuel additives for direct injection gasoline (DIG) injector deposit control. *SAE Technical Papers*, SAE International. 2000. https://doi.org/10.4271/2000-01-2020.

[43] Da Silva MPF, Brito LRE, Honorato FA, Paim APS, Pasquini C, Pimentel MF. Classification of gasoline as with or without dispersant and detergent additives using infrared spectroscopy and multivariate classification. Fuel 2014;116:151–7. https://doi.org/10.1016/j.fuel.2013.07.110.

[44] Yang SQ. Drag reduction in turbulent flow with polymer additives. J. Fluids Eng. Trans. ASME 2009;131(5):0513011–8. https://doi.org/10.1115/1.3111255.

[45] Min T, Yoo JY, Choi H, Joseph DD. Drag reduction by polymer additives in a turbulent channel flow. J Fluid Mech 2003;486(486):213–38. https://doi.org/10.1017/S0022112003004610.

[46] Tsukahara T, Motozawa M, Tsurumi D, Kawaguchi Y. PIV and DNS analyses of viscoelastic turbulent flows behind a rectangular orifice. Int J Heat Fluid Flow 2013;41:66–79. https://doi.org/10.1016/j.ijheatfluidflow.2013.03.011.

[47] Naseri H, Trickett K, Mitroglou N, Karathanassis I, Koukouvinis P, Gavaises M, et al. Turbulence and cavitation suppression by quaternary ammonium salt additives. Sci Rep 2018;8(1). https://doi.org/10.1038/s41598-018-25980-x.

[48] Naseri H, Koukouvinis P, Malgarinos I, Gavaises M. On viscoelastic cavitating flows: a numerical study. Phys Fluids 2018;30(3):033102. https://doi.org/10.1063/1.5011978.

[49] Karathanassis IK, Trickett K, Koukouvinis P, Wang J, Barbour R, Gavaises M. Illustrating the effect of viscoelastic additives on cavitation and turbulence with X-ray imaging. Sci Rep 2018;8(1):14968. https://doi.org/10.1038/s41598-018-32996-w.

[50] Zhu X, Andersson Ö. Performance of new and aged injectors with and without fuel additives in a light duty diesel engine. Transp. Eng. 2020;1:100007. https://doi.org/10.1016/j.treng.2020.100007.

[51] "'Spray G' Operating Condition – Engine Combustion Network" [Online]. Available: https://ecn.sandia.gov/gasoline-spray-combustion/target-condition/spray-g-operating-condition/. [Accessed: 25-Mar-2021].

[52] Karathanassis IK, Koukouvinis P, Kontolatis E, Lee Z, Wang J, Mitroglou N, et al. High-speed visualization of vortical cavitation using synchrotron radiation. J Fluid Mech 2018;838:148–64. https://doi.org/10.1017/jfm.2017.885.

[53] Karathanassis IK, Heidari-Koochi M, Zhang Q, Hwang J, Koukouvinis P, Wang J, et al. X-ray phase contrast and absorption imaging for the quantification of transient cavitation in high-speed nozzle flows. Phys Fluids 2021;33(3):032102. https://doi.org/10.1063/5.0038475.

[54] "Mesh and Geometry – Engine Combustion Network" [Online]. Available: https://ecn.sandia.gov/gasoline-spray-combustion/computational-method/mesh-and-geometry/. [Accessed: 25-Mar-2021].

[55] Andersen VF, Anderson JE, Wallington TJ, Mueller SA, Nielsen OJ, Vapor Pressures of Alcohol-Gasoline Blends, *Energy and Fuels*, American Chemical Society, 2010:3647–54. https://doi.org/10.1021/ef100254w.

[56] Wang L, Wu Z, Ahmed A, Badra JA, Sarathy SM, Roberts WL, et al. Auto-Ignition of direct injection spray of light naphtha, primary reference fuels, gasoline and gasoline surrogate. Energy 2019;170:375–90. https://doi.org/10.1016/j.energy.2018.12.144.

[57] "ASTM D86 - 20b Standard Test Method for Distillation of Petroleum Products and Liquid Fuels at Atmospheric Pressure" [Online]. Available: https://www.astm.org/Standards/D86.htm. [Accessed: 01-Jun-2021].

[58] Otsu N. A threshold selection method from Gray-level histograms. IEEE Trans Syst Man Cybern 1979;9(1):62–6. https://doi.org/10.1109/TSMC.1979.4310076.

[59] Gilles-Birth I, Bernhardt S, Spicher U, Rechs M. A study of the in-nozzle flow characteristic of valve covered orifice nozzles for gasoline direct injection. *SAE Technical Papers*, SAE International 2005. https://doi.org/10.4271/2005-01-3684.

[60] Dubief Y, White CM, Terrapon VE, Shaqfeh ESG, Moin P, Lele SK. On the coherent drag-reducing and turbulence-enhancing behaviour of polymers in wall flows. J Fluid Mech 2004;514:271–80. https://doi.org/10.1017/S0022112004000291.

[61] White CM, Mungal MG. Mechanics and prediction of turbulent drag reduction with polymer additives. Annu Rev Fluid Mech 2008;40(1):235–56. https://doi.org/10.1146/annurev.fluid.40.111406.102156.

[62] Arcoumanis C, Flora H, Gavaises M, Kampanis N, Horrocks R. Investigation of cavitation in a vertical multi-hole injector. *SAE Technical Papers*, SAE International 1999. https://doi.org/10.4271/1999-01-0524.

[63] Aleiferis PG, Serras-Pereira J, van Romunde Z, Caine J, Wirth M. Mechanisms of spray formation and combustion from a multi-hole injector with E85 and gasoline. Combust Flame 2010;157(4):735–56. https://doi.org/10.1016/j.combustflame.2009.12.019.

[64] Mojtabi M, Wigley G, Helie J. The effect of flash boiling on the atomization performance of gasoline direct injection multistream injectors. At. Sprays 2014;24(6):467–93. https://doi.org/10.1615/AtomizSpr.2014008296.

[65] Wu S, Yang S, Wooldridge M, Xu M. Experimental study of the spray collapse process of multi-hole gasoline fuel injection at flash boiling conditions. Fuel 2019;242:109–23. https://doi.org/10.1016/j.fuel.2019.01.027.

[66] Kook S, Pickett LM, Musculus MPB. Influence of diesel injection parameters on end-of-injection liquid length recession. SAE Technical Papers, SAE International 2009;2(1):1194–210. https://doi.org/10.4271/2009-01-1356.

[67] Manin J, Bardi M, Pickett LM, Dahms RN, Oefelein JC. Microscopic investigation of the atomization and mixing processes of diesel sprays injected into high pressure and temperature environments. Fuel 2014;134:531–43. https://doi.org/10.1016/j.fuel.2014.05.060.

[68] Swantek AB, Duke D, Tilocco FZ, Sovis N, Powell CF, Kastengren AL. End of Injection, Mass Expulsion Behaviors in Single Hole Diesel Fuel Injectors. Proceedings of ILASS Americas. 2014.
[69] Pos R, Avulapati M, Wardle R, Cracknell R, Megaritis T, Ganippa L. Combustion of ligaments and droplets expelled after the end of injection in a multi-hole diesel injector. Fuel 2017;197:459–66. https://doi.org/10.1016/j.fuel.2017.02.048.
[70] Goldin M, Pfeffer R, Shinnar R. Break-up of a capillary jet of a non-newtonian fluid having a yield stress. Chem Eng J 1972;4(1):8–20. https://doi.org/10.1016/0300-9467(72)80048-0.
[71] Keshavarz B, Houze EC, Moore JR, Koerner MR, McKinley GH. Ligament mediated fragmentation of viscoelastic liquids. Phys Rev Lett 2016;117(15):154502. https://doi.org/10.1103/PhysRevLett.117.154502.